

1 **Digital Navigation of Energy–Structure–Function Maps for Hydrogen-Bonded** 2 **Porous Molecular Crystals**

3

4 Chengxi Zhao,^{1,2} Linjiang Chen,^{*,2,3} Yu Che,² Zhongfu Pang,² Xiaofeng Wu,^{2,3} Yunxiang Lu,¹ Honglai
5 Liu,¹ Graeme M Day,^{*,4} and Andrew I. Cooper ^{*,2,3}

6

7 1. Key Laboratory for Advanced Materials and School of Chemistry and Molecular Engineering, East
8 China University of Science and Technology, Shanghai, China.

9 2. Leverhulme Research Centre for Functional Materials Design, Materials Innovation Factory and
10 Department of Chemistry, University of Liverpool, Liverpool, UK.

11 3. Key Laboratory for Advanced Materials and Joint International Research Laboratory of Precision
12 Chemistry and Molecular Engineering, Feringa Nobel Prize Scientist Joint Research Centre, School of
13 Chemistry and Molecular Engineering, East China University of Science and Technology, Shanghai,
14 China.

15 4. Computational Systems Chemistry, School of Chemistry, University of Southampton, Southampton,
16 UK.

17

18 **Abstract:** Energy–structure–function (ESF) maps can aid the targeted discovery of porous molecular
19 crystals by predicting the stable crystalline arrangements along with their functions of interest. Here, we
20 compute ESF maps for a series of rigid molecules that comprise either a triptycene or a spiro-biphenyl
21 core, functionalized with six different hydrogen-bonding moieties. We show that the positioning of the
22 hydrogen-bonding sites, as well as their number, has a profound influence on the shape of the resulting
23 ESF maps, revealing promising structure–function spaces for future experiments. We also demonstrate a
24 simple and general approach to representing and inspecting the high-dimensional data of an ESF map,
25 enabling an efficient navigation of the ESF data to identify ‘landmark’ structures that are energetically
26 favourable or functionally interesting. This is a step toward the automated analysis of ESF maps, an
27 important goal for closed-loop, autonomous searches for molecular crystals with useful functions.

28

29 **Introduction**

30 Hydrogen bonding is widely used for controlling supramolecular assembly of organic building blocks^{1,2}
31 because it is directional and relatively strong for a non-covalent interaction. Molecules that combine
32 hydrogen-bonding interactions and geometries that hinder close packing are known to promote porosity
33 in crystalline molecular networks.^{3,4,5,6} Indeed, there is a rapidly growing class of hydrogen-bonded
34 organic frameworks (HOFs) with potential applications in gas storage and separation,^{7,8} molecular
35 recognition,^{9,10} ion conduction,^{11,12} and catalysis.¹³

36

37 Porous bonded frameworks such as metal–organic frameworks (MOFs) and covalent organic
38 frameworks (COFs) are assembled according to strong and predictable bonding patterns.¹⁴ By contrast,
39 porous molecular crystals are defined by the balance of many weak intermolecular interactions, such as
40 hydrogen bonding and π – π stacking. As a result, small changes to the molecular structure can drastically
41 change the crystalline packing of the molecule and its propensity for polymorphism, as well as the
42 resultant physical properties. It is a long-standing challenge to control the crystallization of organic
43 molecules to achieve specific structures with desired functions. The introduction of hydrogen-bonding
44 groups, such as carboxylic acids, to create directional molecular building blocks or “tectons”¹⁵ is one
45 popular route for this, but such routes may also introduce synthetic complexity or chemical
46 characteristics that are not aligned with the intended function (*e.g.*, rigid, polar polyaromatic molecules
47 can have very poor solubility). In the absence of a predictive understanding of molecular assembly in
48 the solid state, it is challenging to rationally select or design appropriate molecular tectons for the
49 synthesis of new functional molecular crystals—this is in sharp contrast to MOFs and COFs, for
50 example, where intuitive isorecticular design strategies have proved powerful.¹⁴

51

52 Recently, we proposed the concept of energy–structure–function (ESF) maps to aid the discovery of
53 porous molecular crystals with arresting properties.³ To generate ESF maps, we combine crystal
54 structure prediction (CSP), which determines the stable crystalline arrangements that are available to a
55 molecule, with predictions of materials properties of interest. ESF maps, which are constructed using
56 the molecular structure as the only input, reveal the possible structures and properties that are available
57 for the molecule within the energetically accessible regions of its lattice energy surface. This *de novo*
58 strategy of exploring potential molecules using their predicted ESF maps is therefore applicable to both
59 known and hypothetical molecules, and to any materials properties that can be computed from crystal
60 structures such as gas adsorption and charge transport.¹⁶ ESF maps can also be used to computationally
61 pre-screen multiple candidate molecules for target applications to focus experimental efforts, which can
62 often require months of synthetic work to access new molecular tectons. ESF maps have been shown to
63 help guide synthetic control over pore size in isostructural porous organic cages¹⁷⁻¹⁹ and to enable the
64 discovery of new ‘hidden’ porous polymorphs of trimesic acid and adamantane-1,3,5,7-tetracarboxylic
65 acid, two archetypal molecules that had been studied for decades by crystal engineers.²⁰ The potential of

66 small organic molecules to give rise to promising molecular photocatalysts¹³ and electronics^{16,21} may
67 also be evaluated *a priori* by ESF maps.

68

69 Going forward, the fast yet accurate generation of ESF maps, as well as visualization and interpretation
70 of the data, will require further development of techniques in fields that span computational chemistry,
71 machine learning, and algorithms. First, the computational expense involved with CSP increases
72 dramatically with the size and complexity of the molecule. For example, large, flexible molecules
73 require extensive sampling of their coupled inter- and intra-molecular phase spaces in the search of
74 stable crystal structures.^{13,22,23} Second, materials properties that derive from the crystal structure's
75 electronic structure (*e.g.*, band gap) or that require a long system equilibration (*e.g.*, gas selectivity) can
76 be very expensive to evaluate for large numbers of predicted structures, which is commonplace for the
77 CSP landscapes of organic molecules. Third, it is challenging to explore the high-dimensional energetic,
78 structural, and functional landscapes defined by an ESF map – in this respect, they differ from two-
79 dimensional geographical maps.

80

81 Until now, ESF maps have usually been represented by projecting onto their corresponding CSP
82 landscapes; that is, onto a plot of the crystal lattice energy as a function of the crystal density. This has
83 proved powerful in highlighting functionally interesting structures that are also energetically favourable;
84 for example, when there are pronounced local minima that are well separated from the bulk of the CSP
85 landscape, sometimes referred to as “spikes”.³ However, minima, or spikes, in the original high-
86 dimensional ESF space could also be hidden in a simple one-dimensional representation, such as
87 landscapes plotted against the crystal density or the pore surface area. One solution is to generate
88 multiple ESF maps by ‘cutting’ through the ESF space along individual dimensions. Alternatively, more
89 sophisticated structural representations—such as smooth overlap of atomic positions (SOAP)
90 representations of atomic environments^{24,25} and persistent homology barcodes of pore structures²⁶—
91 have been combined with machine learning techniques to learn two-dimensional representations of ESF
92 maps.

93

94 Here, we explored the *in silico* computational design of a series of molecular tectons that comprise
95 either a triptycene or a spiro-biphenyl core, functionalized with various different hydrogen-bonding
96 moieties. Hydrogen bonding and π - π stacking were quantitatively analysed for all the structures on the
97 ESF maps to reveal how the maps evolve based on the different balance of intermolecular interactions in
98 the various tectons. We show that the number of hydrogen bonding sites, as well as their position, has a
99 profound influence on the resulting ESF maps. By applying unsupervised learning to pore descriptors,
100 as well as SOAP representations, two-dimensional embeddings of the high-dimensional ESF data could
101 be learned, which are human interpretable. ESF maps represented in this way enable the navigation of
102 the complex ESF space within a unified framework, rather than using more traditional heuristics.

103

104 **Results**

105 **Crystal structure prediction landscapes**

106 We studied a series of awkwardly shaped molecules with different hydrogen-bonding functionalities
107 (Figure 1, Supplementary Figure 2). Following our previous study,^{3,27} we chose triptycene and spiro-
108 biphenyl cores with the aim of frustrating close packing of the molecules in the solid state. To influence
109 crystal packing, the molecular cores were functionalized by different hydrogen-bonding moieties.
110 Benzimidazolones **T2** and **S2** are included here for comparison; **T2** was shown previously to afford
111 stable, porous crystals. We also studied five six-membered-ring-based hydrogen-bonding moieties: 4-
112 pyridone, 2-pyridone, 2,6(1H,3H)-pyridinedione, 2,4(1H,3H)-pyrimidinedione and 1,4(2H,3H)-
113 pyrazinedione. In combination with the triptycene core, five new molecules were generated: quinolones
114 **TH1** and **TH2**; isoquinolinedione **TH3**; quinazolinediones **TH4** and **TH5** (Figure 1). For the spiro-
115 biphenyl core, only two molecules were considered: quinolone **SH1** and quinazolinediones **SH2**
116 (Supplementary Figure 2). These seven molecules bear different numbers and ratios of hydrogen-bond
117 donors and acceptors, offering a potentially diverse array of options for intermolecular hydrogen
118 bonding and crystal packing.

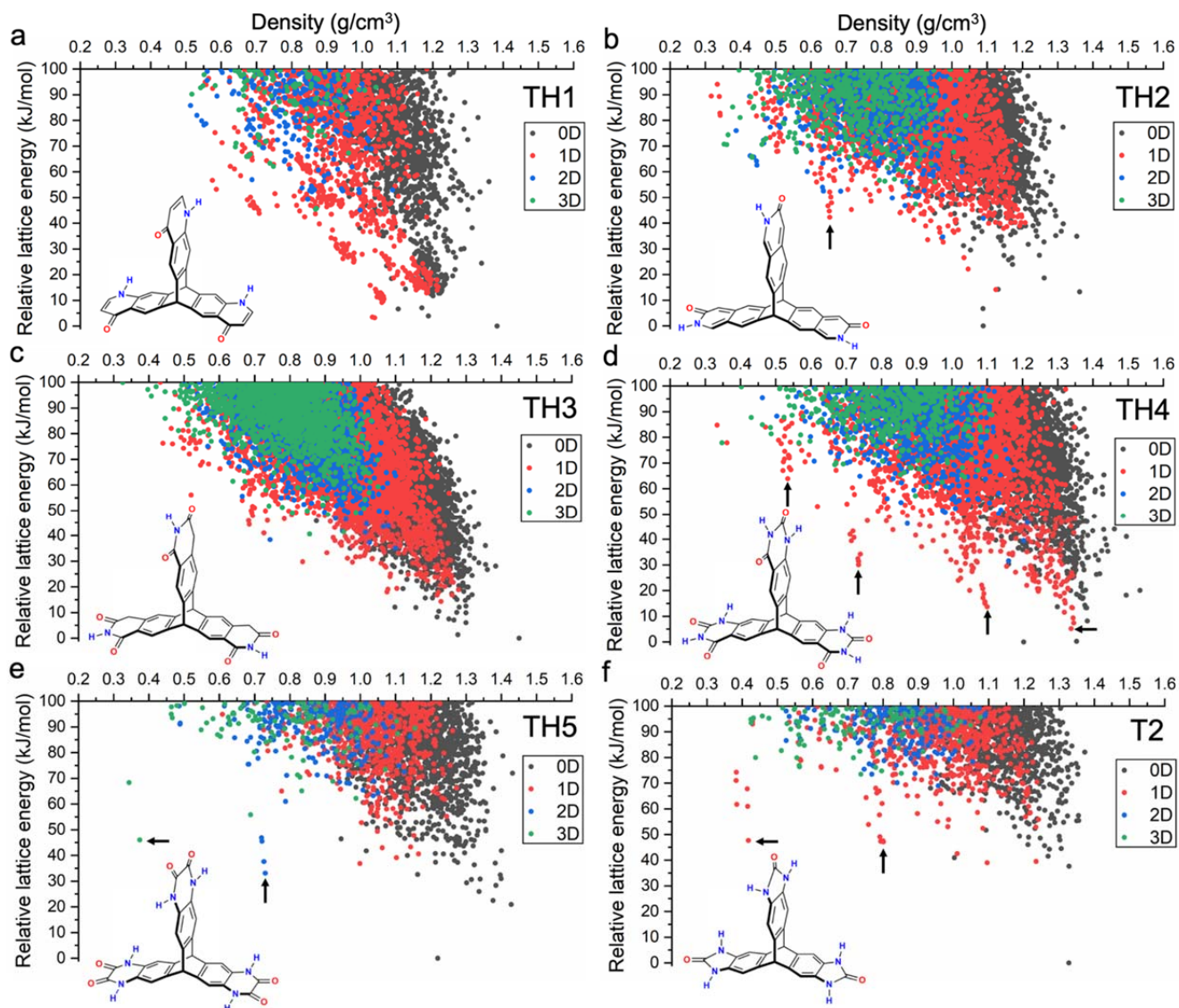
119

120 **TH5** has been synthesized before,²⁸ while **TH1** to **TH4**, **SH1** and **SH2** are, in theory, accessible
121 experimentally via known organic reactions (Supplementary Figures 16–21). However, we envisage that
122 some syntheses might be elaborate and challenging—for example, in terms of isolating specific
123 isomers—and also because these rigid aromatic molecules often have poor solubility. As such,
124 computational pre-screening prior to experiments has significant value. Molecules **TH1** to **TH5**, **SH1**
125 and **SH2** may undergo keto–lactam to enol–lactim tautomerization via intra- or inter-molecular proton
126 transfer. In solution, the lactam–lactim equilibrium is dependent on the solvent polarity, which is shifted
127 to lactam in polar solvents.²⁹ In the solid state, the lactam form is often found to dominate;³⁰ specifically,
128 the molecular arms of **TH1** to **TH5** have been reported in their corresponding lactam form in the
129 Cambridge Structural Database (deposition numbers: 643895, 787295, 1178376, 702449 and 1178443).
130 We did not attempt any organic synthesis in this study, but we offer these systems and the associated
131 predictions as experimental targets for the future.

132

133 Computational methods for crystal structure prediction (CSP) involve a global exploration of the
134 multidimensional lattice energy surface for stable energy minima, followed by an assessment of the
135 relative stabilities of the resulting structures. Here, unbiased searches of the lattice energy surface³¹ were
136 used to determine the stable crystalline arrangements that are available to each of the molecules (Figure
137 1, Supplementary Figure 3). Organic molecules tend to pack densely to maximize their intermolecular
138 interactions, reducing the energetic cost of void space in a solid. As such, generating porosity in
139 molecular crystals remains a challenging task for crystal engineering. Having a rigid and contorted

140 molecular shape may not always be sufficient to prevent dense packing. Indeed, most low-energy
141 structures of triptycene are non-porous and the lower edge of the energy–density distribution decreases
142 nearly monotonically, as is typical for most organic molecules.³ The ‘leading edge’ of a CSP landscape
143 comprises structures with the lowest energy at a given density, and stable porous structures have
144 previously been realized experimentally in this region.³
145



146
147 **Figure 1: Energy–structure–function maps.** a–f, Crystal structure prediction energy–density plots for the
148 molecular building blocks shown in the figure: TH1 (a), TH2 (b), TH3 (c), TH4 (d), TH5 (e) and T2 (f). Each
149 point corresponds to a computed crystal structure. The symbols are colour-coded by the dimensionality of the
150 pore channels, assessed using a probe radius of 1.7Å; see Supplementary Figure 1 for alternative plots with
151 shuffled plotting orders for the points. Molecules TH1–4 each have two isomers arising from the arrangement of
152 the hydrogen-bonding moieties on the triptycene core; only the higher-symmetry isomers were considered here.
153 Arrows indicate the spikes that are referred to in the text.
154

155 The CSP landscape for **T2** is markedly different to that of triptycene, with multiple low-density
156 structures predicted to be substantially lower in energy than the bulk of the landscape, forming the so-
157 called ‘spikes’ (Figure 1f). The emergence of spikes from the bulk of a CSP landscape indicates that the
158 molecule may form unusually stable crystalline structures for their respective densities, and the shape of
159 the energy-density distribution suggests a large energetic barrier separating these structures from higher
160 density regions of the landscape. For **T2**, the minimum-energy structures within the two spikes at
161 densities of about 0.4 g cm^{-3} and 0.8 g cm^{-3} —**T2- γ** and **T2- β** , respectively—can be accessed
162 experimentally by solvent stabilization, even though they are about 50 kJ mol^{-1} above the global energy
163 minimum.³ Despite using a smaller selection of space groups for CSP here than previously (we used 23
164 out of the 89 space groups used in ref 4; see Methods section), the partial energy–density landscape of
165 **T2** shown in Figure 1f captures the same key features as the landscape sampled more exhaustively,
166 including the major ‘spikes’ and the four experimental polymorphs (**T2- σ** , **T2- β** , **T2- γ** and **T2- δ**). We
167 therefore carried out CSP in these 23 space groups for all the other molecules in order to reduce
168 computational costs.

169

170 The leading edge of the energy–density landscape of **TH1** decreases nearly monotonically, with no
171 structures having a density below 0.5 g cm^{-3} located within 100 kJ mol^{-1} above the global energy
172 minimum (Figure 1a). **TH2** is a positional isomer of **TH1**: this arrangement of hydrogen-bonding sites
173 broadens the density distribution of the predicted structure landscape to lower densities and a spike
174 appears at around 0.65 g cm^{-3} (Figure 1b). The isoquinolinedione, **TH3**, has one extra carbonyl group
175 per arm compared to **TH1** and **TH2**, and a methylene unit in the 6-membered ring. The addition of three
176 additional hydrogen-bond accepting groups in **TH3** with respect to **TH2** does not seem to promote low-
177 density, stable structures (Figure 1c). By contrast, the energy–density distribution for **TH4** (Figure 1d)
178 is reminiscent of that for **T2** (Figure 1f) and shows multiple low-energy spikes. Three spikes are
179 apparent at densities of about 0.5 g cm^{-3} , 0.7 g cm^{-3} , and 1.1 g cm^{-3} , which are 63.9 kJ mol^{-1} , 30.0 kJ
180 mol^{-1} , and 13.6 kJ mol^{-1} above the global energy minimum, respectively. By analogy with **T2**, these
181 structures fall in an energy range that we would expect might be accessible via solvent stabilization. **T2**
182 does not have any predicted structures with one-dimensional (1D) channels (red points in Figure 1)
183 within 30 kJ mol^{-1} above the global minimum (Figure 1f; see also Figure 2c in ref 4). By contrast, the
184 plot for **TH4** shows a significant number of structures with 1D pore channels in the density range 1.25 –
185 1.35 g cm^{-3} ; the minimum-energy structure among these is just 5.1 kJ mol^{-1} above the global minimum.
186 The spikes on the landscape of **TH4** can also be recognized at similar density regions on the landscape
187 of **TH2**, although they are less pronounced. Among the four triptycene-based molecules, the positioning
188 of the hydrogen-bonding groups (**TH2** vs. **TH1**) appears to play a more significant role in promoting
189 porosity than their number (**TH2** vs. **TH3**).

190

191 **TH5** is a positional isomer of **TH4** and has a higher point symmetry of D_{3h} (*c.f.*, C_{3v} for **TH4**). Two
192 pronounced spikes emerge from the landscape at densities of about 0.35 g cm^{-3} and 0.7 g cm^{-3} (Figure
193 1e), with the minimum-energy structure in the lowest density spike being only 46.0 kJ mol^{-1} above the
194 global energy minimum. This energy gap is comparable to that (47.6 kJ mol^{-1}) for the lowest-density
195 experimental polymorph of **T2**, **T2- γ** (minimum-energy structure in the spike at 0.5 g cm^{-3}), indicating
196 the possibility of realizing this low-density structure of **TH5**. In contrast to **TH2**, **TH4** and **T2**, where
197 the spikes mainly contain structures with 1D pore channels, structures in the spikes for **TH5** show
198 higher (2D or 3D) pore connectivity (Figure 1e).

199

200 The energy–density landscapes for **SH1** and **SH2** (Supplementary Figure 3) show far fewer predicted
201 structures within 100 kJ mol^{-1} of the global energy minimum than their triptycene counterparts bearing
202 the same hydrogen-bonding motifs (**TH2** and **TH4**, respectively). Likewise, **S2**, having the same
203 hydrogen-bonding moieties as **T2**, does not show unusually stable low-density structures. This suggests
204 that spiro-linked tetrahedral geometries are less effective at generating porosity.

205

206 **Hydrogen bonds stabilize porous structures**

207 Analysis of the intermolecular hydrogen bonding in the leading-edge **T2** structures revealed that
208 structures within the spikes feature hydrogen bonded networks with 2D rings propagating along a third
209 direction to form one-dimensional pore channels.³ Here, we set out to perform quantitative analyses of
210 the hydrogen bonding in the predicted structures of all the molecules studied here (Figure 2a,c,e and
211 Supplementary Figure 4). A hydrogen bond is defined here for an interacting system of three atoms N–
212 H•••O—where, the hydrogen atom (H) is covalently bonded to the nitrogen atom (N) and is interacting
213 with the oxygen atom (O)—when the distance between H and O is shorter than the sum of their van der
214 Waals radii minus 0.1 \AA and the angle formed by N–H•••O, centred on H, is larger than 100° .³

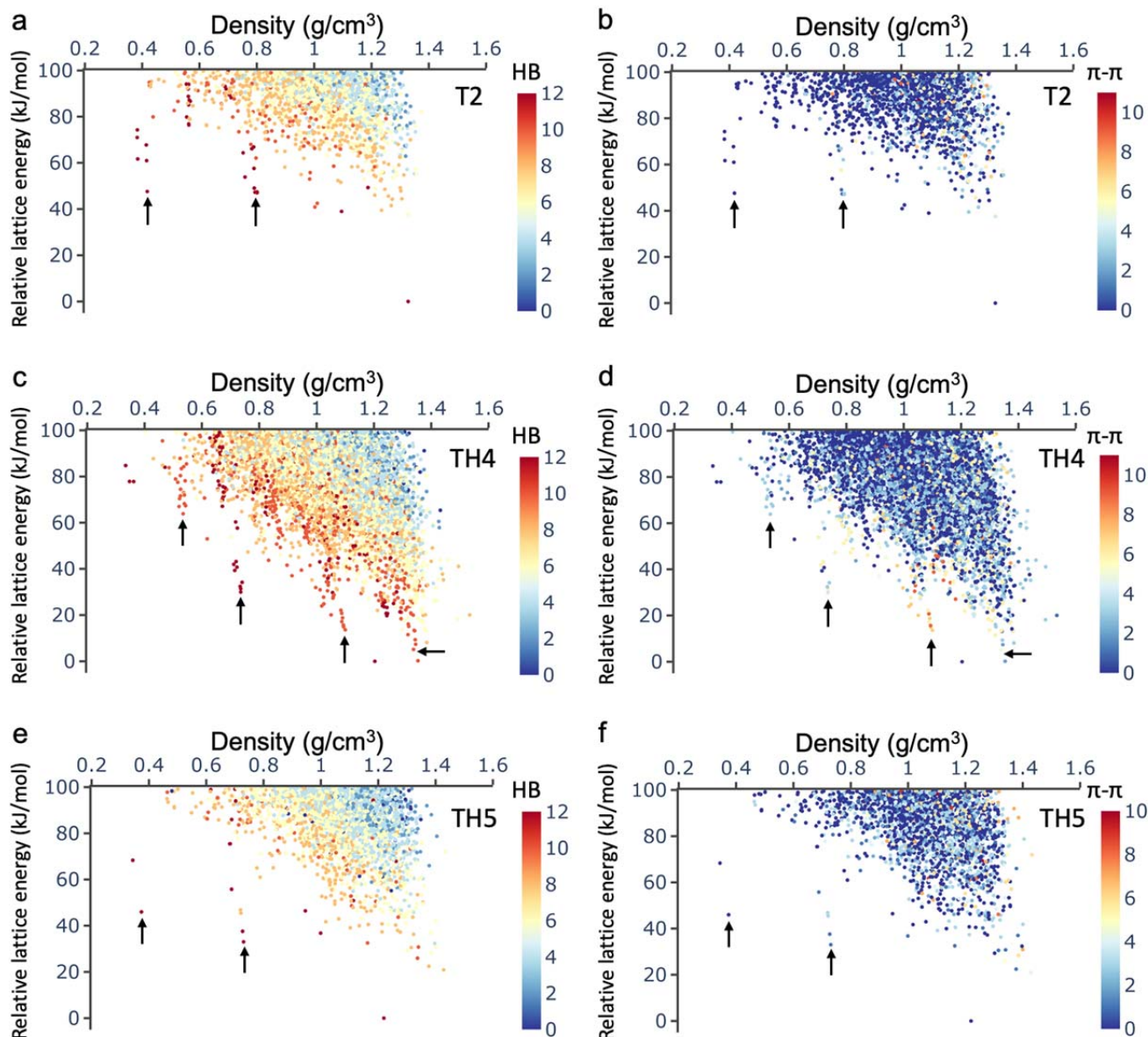
215

216 Figure 2a,c,e shows the CSP landscapes of **T2**, **TH4** and **TH5**, colour-coded by the number of hydrogen
217 bonds each molecule forms in the corresponding crystal structure; this number is (by definition) the
218 same for all the molecules in a given crystal structure because only one unique molecule was considered
219 in these CSP calculations ($Z' = 1$). The analogous results for the other molecules studied are shown in
220 Supplementary Figure 4. The number of hydrogen bonds for a molecule accounts for both cases when
221 carbonyl groups act as a hydrogen-bond acceptor and when N-H groups act as a hydrogen-bond donor.
222 For example, the maximum value of the number of hydrogen bonds for a single **T2** molecule is 12: that
223 is, the six N–H groups can each participate in one hydrogen bond, while the three O atoms can each
224 participate in two hydrogen bonds. In a similar way, we also quantified the extent of intermolecular
225 stacking in each predicted crystal structure (Figure 2b,d,f and Supplementary Figure 5) by counting the
226 π – π stacking modes formed between the arms of the various molecules. Here, we only consider co-
227 facial and parallel-displaced stacking conformations but not T-shaped ones.

228

229 Across the whole series of molecules, intermolecular hydrogen-bonding and intermolecular stacking
230 (see Methods section for the specific definitions used in this study) are found to be mostly competing or
231 orthogonal forces in driving the solid-state packing of these molecules (Figure 2 and Supplementary
232 Figures 4, 5): that is, most structures—particularly in the bulk of the CSP landscape—do not
233 simultaneously show a large number of hydrogen bonds and a large number of π -stacked molecular
234 arms. This results from the positioning of the hydrogen-bonding motifs in the molecule, together with
235 the contorted molecular core. However, this simple picture is more mixed for structures that are close to
236 the leading edge of the landscape or within the spikes. For **T2** and **TH5**, such structures are primarily
237 stabilized by extensive hydrogen bonding (Figure 2a,e), except for some **T2** structures in the medium
238 density range (around 0.8 g cm^{-3}) that show enhanced but still moderate stacking between the molecular
239 arms (Figure 2b). By contrast, the leading-edge structures of **TH4** benefit from both strong hydrogen
240 bonding *and* moderate to strong molecular stacking (Figure 2c,d), except for the lowest-density spike ($<$
241 0.4 g cm^{-3}) where structures only exhibit strong hydrogen bonding. For all the molecules, densely
242 packed structures in the bulk of the landscape are characterized by increased levels of intermolecular
243 stacking and decreased levels of intermolecular hydrogen bonding. The conclusions for the spiro-linked
244 **SH1**, **SH2** and **S2** molecules are broadly the same as for their triptycene analogues (Supplementary
245 Figures 4 and 5).

246



247

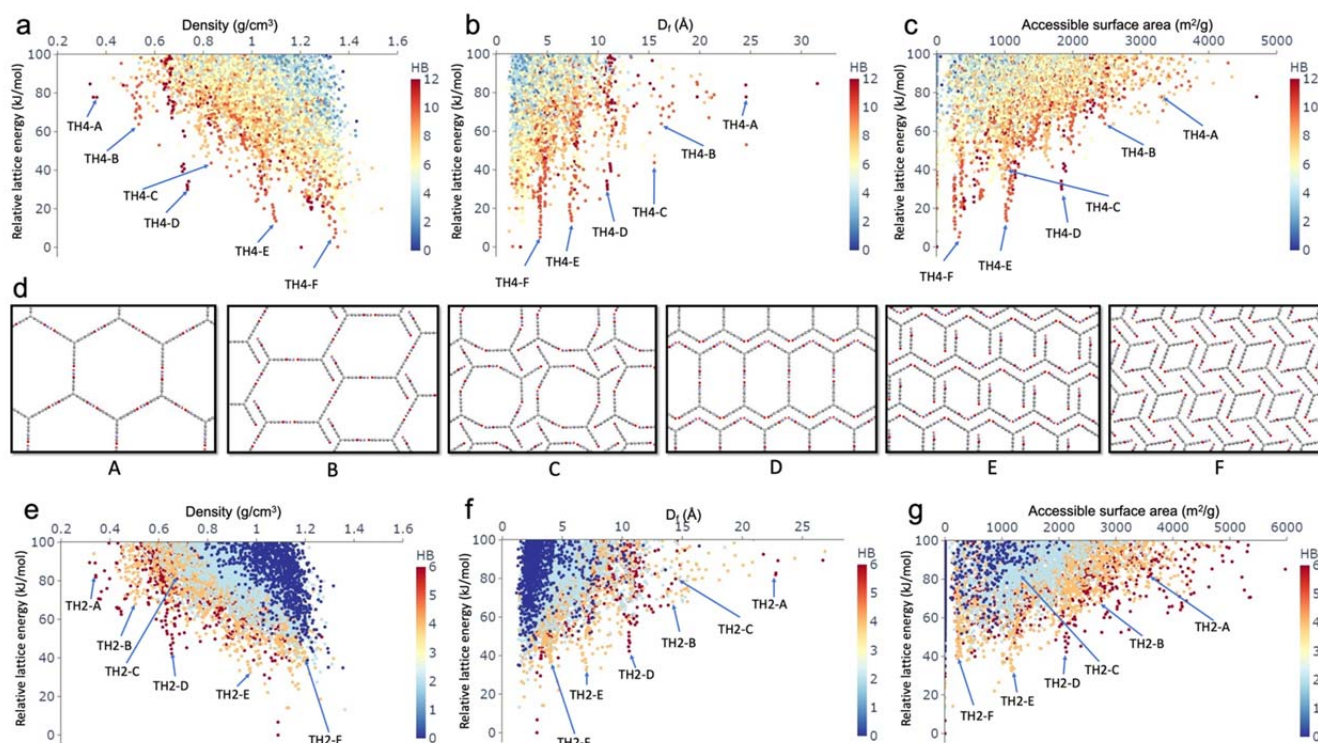
248 **Figure 2: ESF maps for intermolecular hydrogen bonding and intermolecular stacking.** CSP energy–density
 249 landscapes, colour-coded by the number of intermolecular hydrogen bonds (HB; a, c and e) or the number of
 250 intermolecular stacking modes (π – π ; b, d and f; defined as face-to-face stacking between two molecular arms)
 251 formed by one molecule with its neighbours in the crystal structure: **T2** (a,b), **TH4** (c,d) and **TH5** (e,f). Arrows
 252 indicate the spikes that are referred to in the text.

253

254 **ESF data mapped onto individual structural descriptors**

255 Energy–structure–function (ESF) maps combine crystal structure prediction (CSP), which determines
 256 the stable crystalline arrangements available to a molecule, with predictions of materials properties of
 257 interest, using the molecular structure as the only input (see Methods section for details).
 258 Conventionally—and intuitively—ESF maps are projected on their corresponding CSP energy–density
 259 landscapes, with each point on the ‘map’ representing a predicted crystal structure with its colour coded
 260 to one of its physical or functional properties; for example, the pore topologies are colour-coded in

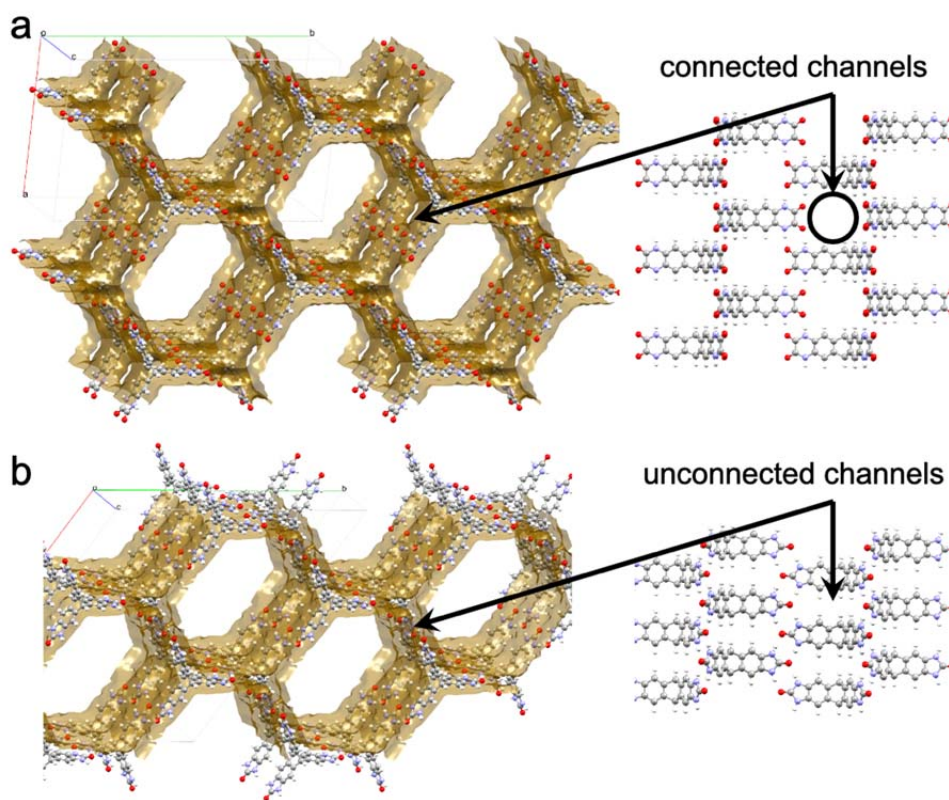
261 Figure 1. This is not the only possible representation: more generally, an ESF map can be projected onto
 262 many different structural parameters. Figure 3 shows ESF maps projected onto three different structural
 263 descriptors: crystal density, largest free sphere diameter, and accessible surface area.
 264



265
 266 **Figure 3: ESF maps for individual structural descriptors.** ESF maps for **TH4** (a–c) and **TH2** (e–g), plotted
 267 against the crystal density (a, e), the largest free sphere diameter (D_f ; b, f) or the accessible surface area (c, g);
 268 symbols are colour-coded by the number of hydrogen bonds formed by each molecule in the crystal structure.
 269 Selected **TH4** ‘landmark’ structures A–F are displayed in (d) and labelled in (a–c), with their **TH2** analogues
 270 labelled in (e–g).

271
 272 For **TH4**, spikes emerge from the bulk of the landscape on all three ESF maps, as shown in Figure 3a–c.
 273 Low-energy structures within these spikes show complete or almost complete saturation of the
 274 hydrogen-bonding sites of the **TH4** molecule, showing that extensive intermolecular hydrogen bonding
 275 serves to facilitate stable porous structures. The minimum-energy structure of each pronounced spike in
 276 the energy–density landscape is shown in Figure 3d; these structures are also found on the leading edge
 277 of the landscape when plotted against the largest free sphere diameter (Figure 3b) or the accessible
 278 surface area (Figure 3c). These landmark structures (Figure 3d; A–F) all exhibit extended hydrogen-
 279 bonded chains along the pore channels. In **TH4-A**, molecules pack ‘head-to-head’ to form two
 280 dimensional layers, using the hydrogen-bonding sites at the tip of each arm (Supplementary Figure 6a);
 281 these layers stack along the third direction, forming linear hydrogen bonds between the edges of the
 282 molecules. Similar hydrogen-bonding patterns also appear in the other landmark structures (Figure 3d),

283 with stacking between the molecular arms becoming more extensive as the structure gets denser
284 (Supplementary Figure 6).
285



286
287 **Figure 4: ESF maps predict a highly porous solid for TH5.** Solvent accessible surfaces (left) of **TH5-A** (a) and
288 **T2- γ** (b). **TH5-A** shows a three-dimensionally interconnected pore space within the structure. Unlike for **T2- γ** ,
289 the 1D hexagonal pore channels in **TH5-A** are predicted to be connected by apertures in the pore walls that are
290 orthogonal to the direction of the channels; one such aperture is indicated by the black circle on the right-hand-
291 side figure. Predicted surface area for **TH5-A** = 4447 m² g⁻¹ (*c.f.*, 3199 m² g⁻¹ predicted for **T2- γ**).

292
293 **TH5** is predicted to yield landmark structures **A**, **B**, **C1** and **D2** (Supplementary Figure 8) that are
294 isostructural with **TH2/4-A** to **D**, respectively, in terms of the 1D channel shapes. In contrast with
295 **TH2/4-A** having 1D pore channels, the 1D channels in **TH5-A** are interconnected through apertures in
296 the pore ‘walls’, as a result of the packing of **TH5** molecules along the channel direction (Figure 4).
297 Similarly, interconnected 1D channels are present in other **TH5** landmark structures, such as **B**, **C1**, **C2**,
298 **D1** and **D2** (Supplementary Figure 9). **TH5-A** has a predicted density of just 0.374 g cm⁻³, with a
299 calculated accessible surface area of 4447 m² g⁻¹, assessed by a probe radius of 1.70 Å. This highly
300 porous structure might be accessible in the laboratory because it is isostructural to **T2- γ** , which has been
301 isolated,^{3,27} and it is predicted to have a similar relative stability (46.0 and 47.6 kJ mol⁻¹ above the
302 corresponding global minimum for **TH5-A** and **T2- γ** , respectively). If it can be prepared and it is stable
303 to desolvation, **TH5-A** would be one of the lowest density molecular crystals reported to date. Few (if

304 any) desolvated molecular crystals have densities lower than 0.4 g cm^{-3} . Two triptycene-based
305 hydrogen-bonded organic frameworks, reported by Stoddart and co-workers,^{32,33} showed ultra-low
306 framework densities of 0.323 or 0.231 g cm^{-3} , but both of the solved crystal structures were for solvates.
307 One of these crystals was reported to have a theoretical surface area of $1690 \text{ m}^2 \text{ g}^{-1}$, although the
308 measured Brunauer–Emmett–Teller surface areas were much lower. We therefore suggest that **TH5-A**
309 has the potential to be the most porous HOF to date, although its very low predicted density implies that
310 careful desolvation might be required; for example, by using solvent exchange protocols or supercritical
311 drying.

312

313 **TH2** gives similar ESF maps to those of **TH4**: spikes emerge from the landscape in the same regions of
314 the structural descriptor used (Figure 3e–g). This is because **TH2** is predicted to generate crystal
315 structures **TH2-A** to **F** that are isostructural with **TH4-A** to **F**, respectively, in terms of the shapes of the
316 one-dimensional pore channels (Figure 3d and Supplementary Figure 7); for example, **TH2-A** and **TH4-**
317 **A** both have hexagonal pore channels. However, in these **TH2** landmark structures, molecules do not
318 pack ‘edge-to-edge’, due to the absence of the hydrogen-bonding sites on the edges of the molecule.
319 Instead, **TH2** molecules tend to form staggered hydrogen-bonded chains along the pore channels: each
320 molecular arm forms hydrogen bonds with two other arms from two different molecules
321 (Supplementary Figure 7). This ‘head-to-tail’ hydrogen-bonding motif,³⁴ labelled “type 2” in
322 Supplementary Figure 7g,h, helps the molecular assembly to extend by repeating the bonding motif.
323 **TH2-A** to **F** are mostly found on the leading edge of the landscape plotted against one of the structural
324 descriptors (Figure 3e–g); **TH2-C** is higher in lattice energy than the corresponding region of the
325 leading edge, for all three ESF maps. In line with the above discussion for **TH4**, **TH2** structures on the
326 leading edge and within the spikes—particularly low-density, large-pore, or large-surface-area ones—
327 exhibit rich intermolecular hydrogen bonding. All six hydrogen-bonding sites on each **TH2** molecule
328 are used in **TH2-A,D**, while four hydrogen-bonding sites are used in **TH2-B,C,E,F**.

329

330 Decomposition of the lattice energy into its physical contributions (Supplementary Figure 10)
331 corroborates the picture built by simple counting of the intermolecular hydrogen bonds and π – π
332 stacking modes. All landmark structures are characterized by strong, stabilizing electrostatic interactions,
333 with the **TH4** structures consistently more stable than their **TH2** counterparts thanks to its larger
334 number of hydrogen-bonding sites than **TH2**. Structures **A**, **B** and **D** bear (nearly) linear hydrogen
335 bonds and hence are stabilized by strongly directional electrostatic interactions, while structures **E** and **F**
336 show enhanced dispersion interactions resulting from increased stacking between the molecular arms.
337 The landmark structures of **TH2** and **TH4** are reminiscent of the experimental polymorphs of **T2**:
338 structures **TH2/4-A**, **C**, **D** and **E** have isostructural pore channels with **T2- γ** , **α** , **β** and **δ** , respectively.
339 Therefore, it is conceivable that these landmark structures—particularly for **TH4**, whose landmark

340 structures are all minimum-energy structures within their corresponding spikes—might be
341 experimentally accessible should this molecule be synthesized in the future.

342

343 To assist with both the analysis in this study and with future interpretations of ESF maps, we developed
344 an interactive visualization tool—an ESF Explorer—using **TH4** as an example here
345 (<https://www.interactive-esf-maps.app>). This tool allows the user to interrogate the correlations,
346 dependencies, and relationships between the various dimensions of the data. In the ESF Explorer, a
347 variety of ‘descriptors’ can be chosen as the X-axis, the Y-axis, and as colour-coding in the ESF map.
348 The predicted crystal structures are displayed interactively when points are selected on the ESF plot.
349 Our interactive visualization tool was inspired by the pioneering efforts of Moghadam *et al.* in exploring
350 high-throughput screening data of metal–organic frameworks.^{35,36}

351

352 **Two-dimensional embeddings of the high-dimensional ESF data**

353 While projecting an ESF map onto individual dimensions is a useful way of exploring data, it can be
354 laborious when many structural and functional properties are associated with 1000s to 10,000s of
355 structures typically on a single ESF map, even with the help of our interactive ESF Explorer. It is
356 therefore desirable to devise a simple and general approach to represent the high-dimensional data of
357 ESF maps, allowing us to systematically identify ‘landmark’ structures on the map, be they either
358 energetically favourable or functionally interesting structures. To do this, we encoded each of the crystal
359 structures on an ESF map by a number of pore descriptors including pore diameters, surface areas and
360 some variants of these in order to capture, to some extent, the heterogeneity of pore/channel sizes within
361 a given map (see Supplementary Methods). We then used the affinity propagation algorithm³⁷ to cluster
362 all the crystal structures into unique groups on the porosity space defined by these pore descriptors. For
363 each group, a landmark structure was identified as the lowest-energy structure within the group; see
364 Figure 5d–g for where these landmarks are located on the corresponding energy–density landscapes.

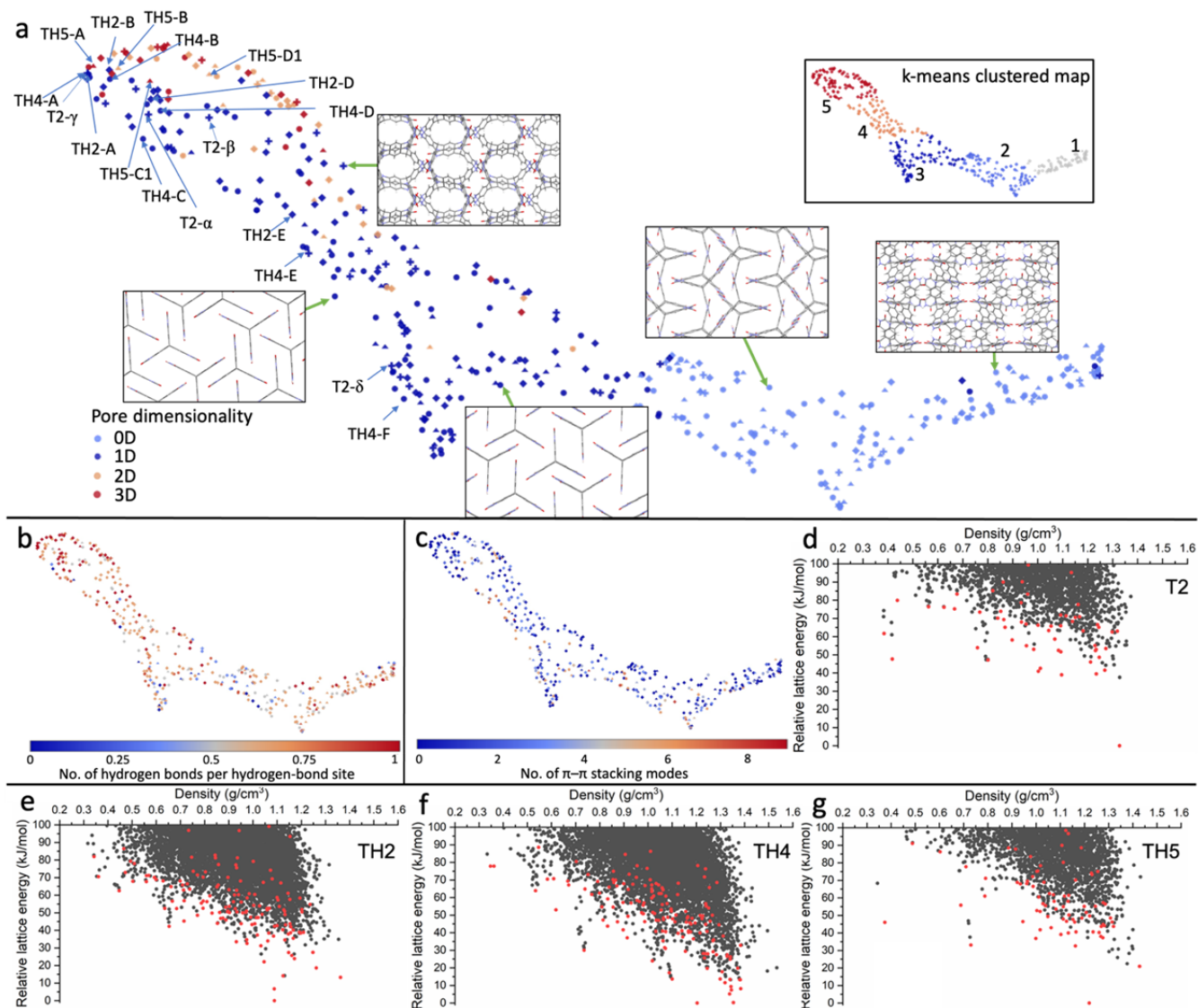
365

366 We identified landmark structures for **TH2**, **TH4**, **TH5** and **T2** following the same protocol. Since our
367 pore descriptors are agnostic to the molecular structure, landmark structures can be compared across the
368 different molecules in a single projection. For visual comparison, we applied the parametric Uniform
369 Manifold Approximation and Projection (UMAP)³⁸ technique to learn a mapping from the high-
370 dimensional porosity space to a 2D representation (Figure 5a), where each point represents a crystal
371 structure and the points are spatially arranged such that the closer the two points are on the plot, the
372 more similar the two structures are in the porosity space. We further used the k-means algorithm³⁹ to
373 identify clusters on the 2D UMAP space, which are superposed on the 2D UMAP plot (inset, Figure 5a).

374

375 All four experimental polymorphs of **T2**, as well as most of the structures highlighted above for **TH2**,
376 **TH4** (Figure 3) and **TH5** (Supplementary Figure 8), were identified as landmarks on the porosity space;

377 note that **TH2-C,F**, and **TH5-C2,D2** are not shown in Figure 5a–c because they are not the
 378 representative structure (in this case, the most stable structure) of their corresponding cluster. The
 379 structures that have isostructural pore channels—for example, **TH2-A**, **TH4-A**, **TH5-A** and **T2- γ** all
 380 have hexagonal pore channels—are located in close proximity on the 2D UMAP representation (Figure
 381 5a). An interactive explorer for the 2D UMAP embeddings of the porosity spaces of **TH2**, **TH4**, **TH5**
 382 and **T2** is available in our online visualization app (<https://www.interactive-esf-maps.app>), which allows
 383 the user to inspect landmark structures identified by having either the lowest lattice energy or the largest
 384 free sphere within the group.
 385



386
 387 **Figure 5: Porosity space of the landmark structures of TH2, TH4, TH5 and T2.** (a–c) 2D UMAP
 388 embeddings of the porosity spaces of **TH2** (diamond), **TH4** (circle), **TH5** (triangle) and **T2** (cross), colour-coded
 389 by the pore dimensionality (a), the number (no.) of hydrogen bonds per hydrogen-bond site (b), or the total
 390 number of π - π stacking modes of the crystal structure (c); the symbol size is scaled by the accessible surface area.
 391 All the points shown in (a–c) are the lowest-energy structures in the respective clusters by affinity propagation

392 and are highlighted in red on their corresponding energy–density landscapes: **T2** (d), **TH2** (e), **TH4** (f) and **TH5**
393 (g).

394

395 Overall, the structures become more porous, with a higher pore dimensionality and/or a larger accessible
396 surface area, when going from the bottom-right to the top-left (or from k-means group 1 to group 5; see
397 inset in Figure 5) of the UMAP embedded porosity space (Supplementary Figure 11). Most landmark
398 structures exhibit extended hydrogen-bonded networks (Figure 5b), while some structures also benefit
399 from a complementary stabilization by π – π stacking interactions (Figure 5c). Results for spiro-linked
400 **SH1**, **SH2** and **S2** are shown in Supplementary Figure 12.

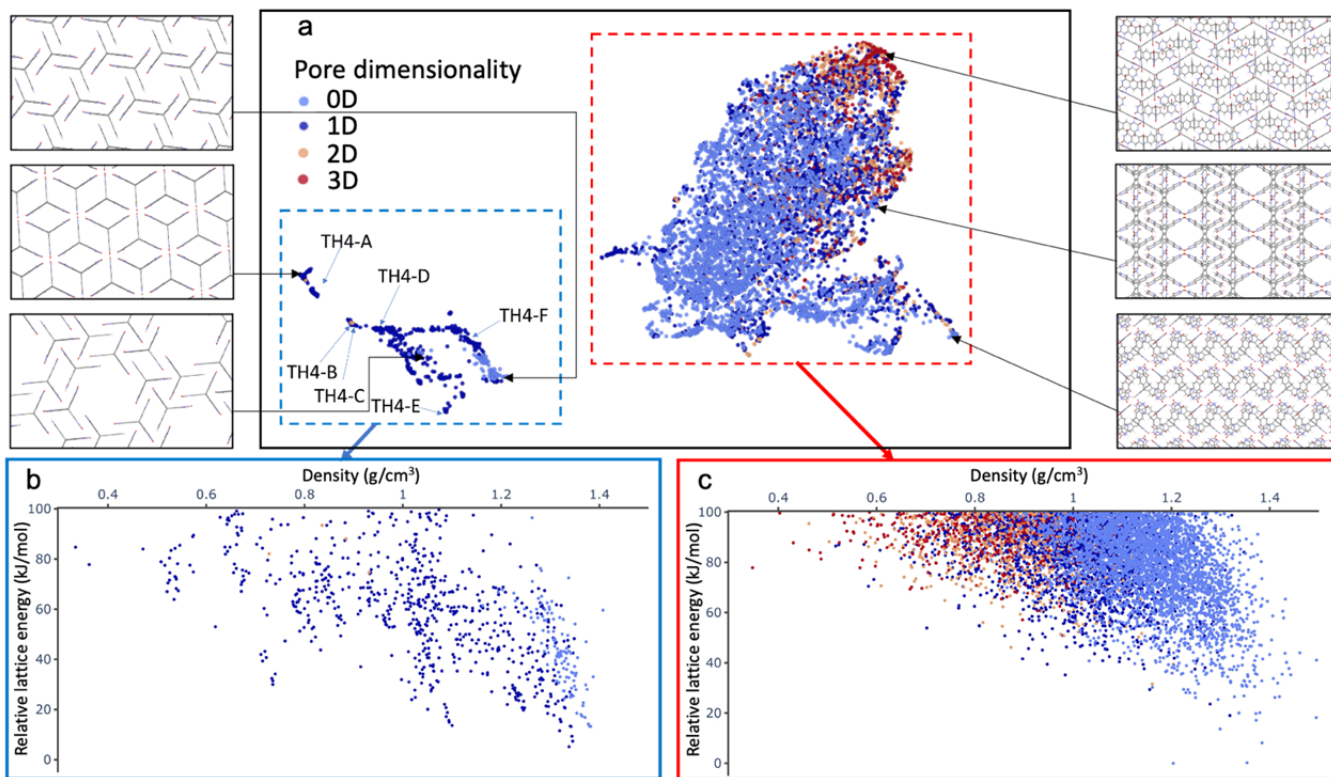
401

402 ESF maps are simplified representations of complex, high-dimensional structure-property landscapes,
403 providing a powerful visualization of the range of properties and stabilities of the associated crystal
404 structures. However, ESF maps can be challenging to interpret, especially as they become more
405 complex. Analogies with geographical maps break down when the structure–property relationships are
406 encoded by a high-dimensional ESF landscape that may have 10,000s of structures on a single map.
407 Inspecting ESF maps by eye is laborious and increasingly intractable as the maps become larger, more
408 numerous, and higher-dimensional. The 2D embedding approach shown here makes ESF maps machine
409 readable. To give one use case: it is often desirable to make comparisons between ESF maps for
410 different molecules to assess whether two molecules will be functionally similar or not. This unified
411 embedding approach will be useful for comparing multiple CSP datasets and identifying functionally
412 similar structures using the encoding representation. This might be used, for example, to select the most
413 synthetically accessible molecule in a set of candidates that is likely to express the property of interest,
414 such as a specific pore size. This approach automatically and systematically identifies a small set of
415 landmark structures (typically, 10's to 100's) from the whole CSP landscape (typically, 1,000's to
416 10,000's structures). This allow us to focus more expensive calculations on a smaller set of structures:
417 for example, to carry out solvent stabilization calculations to better assess the synthetic accessibility of a
418 specific polymorphs. These calculations are too expensive to perform on entire CSP datasets and more
419 simplistic filtering methods (*e.g.*, using a lattice energy cut-off) may miss key landmark structures.

420

421 Simple pore descriptors, such as pore diameters and surface areas, do not have the resolution that is
422 needed to distinguish structures atomistically. By contrast, a range of numerical representations, such as
423 smooth overlap of atomic positions (SOAP),⁴⁰ allow for measuring the similarity between atomistic
424 structures and have been widely used in machine learning tasks.⁴¹ Here, we used SOAP descriptors to
425 encode all the crystal structures of **TH4** and, together with a regularized entropy match (REMatch)
426 kernel,⁴² to quantify the similarity between every pair of structures. The resulting similarity matrix was
427 then projected onto a 2D space by a UMAP embedding, as shown in Figure 6a.

428



429

430 **Figure 6: The ESF data of TH4 mapped onto its SOAP space.** (a) 2D UMAP embedding of the SOAP space
 431 of **TH4**, colour-coded by the pore dimensionality. (b), (c) Energy–density landscapes correspond to the regions
 432 marked out in (a), colour-coded by the pore dimensionality.

433

434 For **TH4**, the crystal structures are split, broadly speaking, into two disconnected ‘islands’ in the SOAP
 435 space (Figure 6a). Both islands contain structures that span the whole density range (Figure 6b,c).
 436 Tracing structures on each island back to the energy–density landscape reveals that the smaller of the
 437 two islands (blue dotted square) is overwhelmingly dominated by structures exhibiting 1D pore
 438 channels (Figure 6b), while the larger island (red dotted square) has a greater number of structures with
 439 different pore dimensionalities (Figure 6c). All the landmark structures, **TH4-A** to **F**, are located on the
 440 smaller, blue island, as well as structures belonging to the spikes and most of the leading-edge structures
 441 on the energy–density landscape (Figure 6b). As discussed above, these structures all feature extended
 442 hydrogen-bonded chains along the 1D channels. Higher-density structures on the blue island show
 443 increased π – π stacking. Almost all structures on the red island are found in the bulk of the energy–
 444 structure landscape, featuring diverse packing patterns, which is understandable as it covers a much
 445 larger area in the SOAP space than the smaller blue island. For **TH5**, the 2D UMAP embedding of the
 446 SOAP space (shown in Supplementary Figure 15) is not clearly separated into ‘islands’ but, like **TH4**,
 447 the leading-edge structures are mostly located in one region of the embedding.

448

449 SOAP descriptors, by design, encode atomic neighbour environments within a cut-off radius, and they
450 are therefore effective at capturing local chemical information such as hydrogen bonding and π - π
451 stacking. A larger cut-off radius of 8.0 Å (Supplementary Figure 14) results in a similar picture to that
452 found with a cut-off radius of 6.0 Å (Figure 6). By contrast, SOAP descriptors have been shown to not
453 capture long-range order, such as molecular packing,²⁶ so these projections are complementary to the
454 pore-based descriptor projections shown in Figure 5.

455

456 Discussion

457 We have computed ESF maps for a series of molecular tectons that comprise either a triptycene or a
458 spiro-biphenyl core, functionalized with various different hydrogen-bonding moieties, evaluating their
459 abilities to generate porosity in the solid state. Through quantitative analyses of the intermolecular
460 hydrogen bonding and π - π stacking for all the predicted crystal structures, we showed how the ESF
461 maps evolve arising from the different balance of intermolecular interactions in the various tectons.
462 Across the whole series of the molecules studied, intermolecular hydrogen bonding and intermolecular
463 stacking are found to be mostly competing forces in driving the solid-state packing of the molecules.
464 That is, high-porosity, low-density structures are primarily stabilized by extensive hydrogen bonding
465 with minimal intermolecular stacking, while densely packed structures exhibit high levels of stacking
466 but decreased levels of hydrogen bonding. Structures in the intermediate density range are stabilized by
467 a combination of hydrogen bonding and stacking. This results from the positioning of the hydrogen-
468 bonding sites, as well as the number of them, and the contorted molecular core. **TH4** and **TH5** have
469 been identified as promising targets for future experimental efforts, because they are both predicted to
470 give multiple (highly) porous crystalline structures that may be experimentally accessible, for example
471 by solvent stabilization. **TH5** has been synthesized before,²⁸ and our results suggest that it would be
472 interesting to re-evaluate this molecule in terms of porosity across a range of crystallization solvents.²⁰

473

474 Inspecting a large and complex multidimensional ESF map can be laborious, even with the help of our
475 interactive ESF Explorer (<https://www.interactive-esf-maps.app>). Here, we have demonstrated a simple
476 and general framework for representing the high-dimensional data of ESF maps and for systematically
477 identifying ‘landmark’ structures on the map. By applying unsupervised learning to pore descriptors, as
478 well as SOAP representations, two-dimensional embeddings of the high-dimensional ESF data could be
479 learned, which are human interpretable. Our approach of encoding, learning, and representing ESP maps
480 enables an efficient navigation of the complex ESF space within a unified framework, allowing us to
481 automatically identify energetically favourable or functionally interesting structures across different
482 systems, as well as revealing complex structure–function correlations that are hidden when inspecting
483 individual structural features. This marks a step toward an automated analysis of high-throughput
484 computation of ESF maps, which will be beneficial in facilitating autonomous searches for functional

485 molecular crystals in the future – for example, to create machine-readable maps to prioritize automated
486 robotic searches.^{43,44}

487

488 **Methods**

489 Crystal structure prediction (CSP)

490 Geometries of all the molecules studied were fully optimized at the B3LYP/6-311G(d,p) level of theory,
491 using the Gaussian16 software,⁴⁵ followed by frequency calculations to ensure that they are all true local
492 minima. These molecular geometries were held rigid throughout crystal structure generation and lattice
493 energy minimization.

494

495 Trial crystal structures were generated with one molecule in the asymmetric unit for the 23 most
496 common space groups: $P2_1/c$ (34.4%), $P\bar{1}$ (24.8%), $C2/c$ (8.4%), $P2_12_12_1$ (7.1%), $P2_1$ (5.1%), $Pbca$
497 (3.3%), $Pna2_1$ (1.4%), $Pnma$ (1.1%), Cc (1.0%), $P1$ (1.0%), $C2$ (0.8%), $Pbcn$ (0.8%), $Pca2_1$ (0.7%), $R\bar{3}$
498 (0.7%), $P2/c$ (0.6%), $C2/m$ (0.5%), $P2_1/m$ (0.5%), Pc (0.4%), $P2_12_12$ (0.4%), $I4_1/a$ (0.4%), $Pccn$ (0.4%),
499 $Fdd2$ (0.3%), and $P4_2$ (<0.3%); the values in the brackets are relative frequencies of the space groups
500 reported in the Cambridge Structural Database.

501

502 CSP was performed using a quasi-random sampling procedure, as implemented in the Global Lattice
503 Energy Explorer software.³¹ The generation of crystal structures involved a low-discrepancy sampling
504 of all structural variables within each space group: unit cell lengths and angles, and molecular positions
505 and orientations within the asymmetric unit. Space-group symmetry was then applied, and a geometric
506 test was performed for overlap between molecules, which was removed by lattice expansion (the SAT-
507 expand method in ref³¹). Lattice energy calculations were performed with an anisotropic atom–atom
508 potential using DMACRYS.⁴⁶ Electrostatic interactions were modelled using an atomic multipole
509 description of the molecular charge distribution (up to hexadecapole on all atoms) from the B3LYP/6-
510 311G(d,p)-calculated charge density using a distributed multipole analysis.⁴⁷ Atom–atom repulsion and
511 dispersion interactions were modelled using a revised Williams intermolecular potential,⁴⁸ which has
512 been benchmarked against accurate, experimentally determined lattice energies for a range of molecular
513 crystals,⁴⁹ and was applied successfully in our earlier CSP studies of **T2** and the related imide **T1**,
514 reproducing the known crystal structures.³ Charge–charge, charge–dipole and dipole–dipole interactions
515 were calculated using Ewald summation; all other intermolecular interactions were summed to a 25-Å
516 cut-off between molecular centres-of-mass. All accepted trial structures were lattice-energy-minimized,
517 and the search was run until a total of 5000 lattice energy minimizations had been performed in each
518 space group.

519

520 Removal of duplicate structures was performed in two steps. First, all structures within a lattice energy
521 window of 1.0 kJ mol⁻¹ and within a density window of ± 0.05 g cm⁻³ were compared using powder x-

522 ray diffraction (PXRD) patterns generated by Platon⁵⁰ (wavelength: 0.7 Å; two-theta range: 20°) using a
523 constrained dynamic time-warping method to compare pairs of structures. Structures were considered a
524 match when the Euclidean distance between the PXRD patterns (normalized by area) was < 10. This
525 was followed by using the COMPACT⁵¹ algorithm for clustering: 1.0 kJ mol⁻¹ and ±0.05 g cm⁻³
526 selection windows; a distance tolerance of 40% and a maximum value of the RMSD of 0.4 Å for 30
527 molecules.

528

529 Pore-geometry analysis

530 Topological analysis of the pore space within a crystal structure was performed using the void analysis
531 tool zeo++.⁵² The outputs from this analysis included the pore dimensionality (0D, 1D, 2D or 3D), pore
532 diameters, surface areas and pore volumes. A probe radius of 1.70 Å was used in all calculations. A total
533 of 18 pore descriptors were used to describe the porosity space of the predicted crystal structures, with
534 full details of their definitions given in the Supplementary Methods. These 18 descriptors are simple
535 extensions to four basic pore descriptors: crystal density, largest pore diameter, total surface area and
536 total pore volume. First, the total surface area and the total pore volume were decomposed into
537 accessible and non-accessible contributions. Second, to capture some extent of the heterogeneity of the
538 pore geometry within a structure, several descriptors were derived based on the surface areas and pore
539 volumes of individual channels and pockets. We found that this set of descriptors satisfactorily captured
540 different pore shapes, such as those having multiple channels with different pore widths or having both
541 channels and pockets.

542

543 Hydrogen-bond and π - π stacking analysis

544 For each predicted crystal structure, hydrogen bonds were identified with the following limits on
545 geometry: $r_{H\cdots A} < [\text{sum}(\text{van der Waals radii}^{53} \text{ of H and A})] - 0.1$ in Å and $\angle D-H\cdots A > 100^\circ$, where D
546 and A are the hydrogen-bond donor and acceptor atoms, respectively. Intermolecular stacking was
547 quantified as the number of face-to-face π - π stacking between two molecular arms, which was
548 identified by the distance between the centroids of two neighbouring aromatic rings being less than 4.4
549 Å and the dihedral angle between the two ring planes being less than 35°. The CSD Python Application
550 Programming Interface, together with in-house scripts, was used to perform these analyses.

551

552 Visualization of the porosity space and the SOAP space

553 The Uniform Manifold Approximation and Projection (UMAP) technique was used for dimensionality
554 reduction for mapping high-dimensional data to 2D representations, while preserving both global and
555 local topological structures of the data in the high-dimensional space as much as possible. That is, the
556 points are arranged spatially such that the closer the two points are on the 2D plot, the more similar the
557 two molecules are, as described by the encoding descriptors. For the porosity spaces (Figure 5a,
558 Supplementary Figures 11–13), the pairwise distances between crystal structures were computed as the

559 Euclidean distances between vectors of the pore descriptors. For the SOAP spaces (Figure 6,
560 Supplementary Figures 14–15), SOAP descriptors were generated for all atoms in the crystal structure,
561 using the DDescribe package.⁵⁴ The regularized entropy match (REMatch)⁴² kernel was used to measure
562 global similarity between crystal structures from SOAP-encoded local atomic environments.

563

564 **Data availability**

565 All the predicted crystal structures and properties are available at
566 <https://doi.org/10.5258/SOTON/D1602>. Data for the ESF maps of **TH4**, as well as data for the 2D
567 embedded porosity spaces and SOAP spaces of **TH2**, **TH4**, **TH5** and **T2**, can be visualized online at
568 <https://www.interactive-esf-maps.app>.

569

570 **Code availability**

571 Python scripts to create interactive visualization tools, like the ESF Explorer shown in this study, are
572 available at https://github.com/Yuchees/esf_explorer_templates.⁵⁵

573

574 **Acknowledgments**

575 We acknowledge the Leverhulme Trust *via* the Leverhulme Research Centre for Functional Materials
576 Design for funding. C.Z. acknowledges the financial support from the China Scholarship Council (No.
577 201806740038). We thank Dr. Peter R Spackman and Dr. Marc A. Little for useful discussions.

578

579 **Author contributions**

580 C.Z. performed the crystal structure predictions, structural analyses, and descriptor calculations. C.Z.
581 and Y.C. performed the unsupervised learning tasks. Y.C. developed and deployed the online
582 application for interactive data visualization. Z.P. proposed the potential synthetic routes and advised
583 C.Z. on crystal structure prediction. X.W. contributed to the interpretation of data and to the
584 implementation of the web-based visualization application; Y.L. and H.L. contributed to the discussions.
585 L.C., A.I.C. and G.M.D. conceived the project; L.C. supervised the project. L.C., C.Z. and A.I.C. led the
586 writing of the manuscript with contributions from all co-authors.

587

588 **Corresponding authors**

589 L.C.: lchen@liverpool.ac.uk; G.M.D.: g.m.day@soton.ac.uk; A.I.C.: aicooper@liverpool.ac.uk.

590

591 **Competing interests**

592 The authors declare no competing interests.

593

594

595 **References**

- 596 1 González-Rodríguez, D. & Schenning, A. P. Hydrogen-bonded supramolecular π -functional
597 materials. *Chem. Mater.* **23**, 310-325 (2011).
- 598 2 Lin, R.-B. *et al.* Multifunctional porous hydrogen-bonded organic framework materials. *Chem.*
599 *Soc. Rev.* **48**, 1362-1389 (2019).
- 600 3 Pulido, A. *et al.* Functional materials discovery using energy–structure–function maps. *Nature*
601 **543**, 657-664 (2017).
- 602 4 Li, P., Ryder, M. R. & Stoddart, J. F. Hydrogen-Bonded Organic Frameworks: A Rising Class of
603 Porous Molecular Materials. *Acc. Mater. Res.* **1**, 77-87 (2020).
- 604 5 Kohl, B., Rominger, F. & Mastalerz, M. Crystal structures of a molecule designed not to pack
605 tightly. *Chem. Eur. J.* **21**, 17308-17313 (2015).
- 606 6 Hisaki, I., Xin, C., Takahashi, K. & Nakamura, T. Designing Hydrogen - Bonded Organic
607 Frameworks (HOFs) with Permanent Porosity. *Angew. Chem. Int. Ed.* **58**, 11160-11170 (2019).
- 608 7 Yang, W. *et al.* Exceptional thermal stability in a supramolecular organic framework: porosity
609 and gas storage. *J. Am. Chem. Soc.* **132**, 14457-14469 (2010).
- 610 8 He, Y., Xiang, S. & Chen, B. A microporous hydrogen-bonded organic framework for highly
611 selective C₂H₂/C₂H₄ separation at ambient temperature. *J. Am. Chem. Soc.* **133**, 14570-14573
612 (2011).
- 613 9 Li, P. *et al.* A homochiral microporous hydrogen-bonded organic framework for highly
614 enantioselective separation of secondary alcohols. *J. Am. Chem. Soc.* **136**, 547-549 (2014).
- 615 10 Yang, S. J., Cho, J. H., Oh, G. H., Nahm, K. S. & Park, C. R. Easy synthesis of highly nitrogen-
616 enriched graphitic carbon with a high hydrogen storage capacity at room temperature. *Carbon*
617 **47**, 1585-1591 (2009).
- 618 11 Xing, G., Yan, T., Das, S., Ben, T. & Qiu, S. Synthesis of crystalline porous organic salts with high
619 proton conductivity. *Angew. Chem. Int. Ed.* **57**, 5345-5349 (2018).
- 620 12 Chen, S. & Zeng, X. C. Design of ferroelectric organic molecular crystals with ultrahigh
621 polarization. *J. Am. Chem. Soc.* **136**, 6428-6436 (2014).
- 622 13 Aitchison, C. M. *et al.* Photocatalytic proton reduction by a computationally identified,
623 molecular hydrogen-bonded framework. *J. Mater. Chem. A* **8**, 7158-7170 (2020).
- 624 14 Yaghi, O. M. Reticular chemistry in all dimensions. *ACS Cent. Sci.* **5**, 1295-1300 (2019).
- 625 15 Brunet, P., Simard, M. & Wuest, J. D. Molecular tectonics. Porous hydrogen-bonded networks
626 with unprecedented structural integrity. *J. Am. Chem. Soc.* **119**, 2737-2738 (1997).
- 627 16 Campbell, J. E., Yang, J. & Day, G. M. Predicted energy–structure–function maps for the
628 evaluation of small molecule organic semiconductors. *J. Mater. Chem. C* **5**, 7574-7584 (2017).
- 629 17 Slater, A. G. *et al.* Computationally-guided synthetic control over pore size in isostructural
630 porous organic cages. *ACS Cent. Sci.* **3**, 734-742 (2017).
- 631 18 Bernabei, M., Pérez-Soto, R., García, I. G. & Haranczyk, M. In silico design and assembly of cage
632 molecules into porous molecular materials. *Mol. Syst. Des. Eng.* **3**, 942-950 (2018).
- 633 19 Garcia, I. G., Bernabei, M., Soto, R. I. P. r. & Haranczyk, M. Out-of-oblivion cage molecules and
634 their porous crystalline phases. *Cryst. Growth Des.* **17**, 5614-5619 (2017).
- 635 20 Cui, P. *et al.* Mining predicted crystal structure landscapes with high throughput crystallisation:
636 old molecules, new insights. *Chem. Sci.* **10**, 9988-9997 (2019).

- 637 21 Cheng, C. Y., Campbell, J. E. & Day, G. M. Evolutionary chemical space exploration for functional
638 materials: computational organic semiconductor discovery. *Chem. Sci.* **11**, 4922-4933 (2020).
- 639 22 Thompson, H. P. & Day, G. M. Which conformations make stable crystal structures? Mapping
640 crystalline molecular geometries to the conformational energy landscape. *Chem. Sci.* **5**, 3173-
641 3182 (2014).
- 642 23 Vasileiadis, M., Pantelides, C. C. & Adjiman, C. S. Prediction of the crystal structures of axitinib,
643 a polymorphic pharmaceutical molecule. *Chem. Eng. Sci.* **121**, 60-76 (2015).
- 644 24 Musil, F. *et al.* Machine learning for the structure–energy–property landscapes of molecular
645 crystals. *Chem. Sci.* **9**, 1289-1300 (2018).
- 646 25 Yang, J. *et al.* Large-Scale Computational Screening of Molecular Organic Semiconductors Using
647 Crystal Structure Prediction. *Chem. Mater.* **30**, 4361-4371 (2018).
- 648 26 Moosavi, S. M., Xu, H., Chen, L., Cooper, A. I. & Smit, B. Geometric landscapes for material
649 discovery within energy–structure–function maps. *Chem. Sci.* **11**, 5423-5433 (2020).
- 650 27 Mastalerz, M. & Oppel, I. M. Rational construction of an extrinsic porous molecular crystal with
651 an extraordinary high specific surface area. *Angew. Chem. Int. Ed.* **51**, 5252-5255 (2012).
- 652 28 Mastalerz, M., Sieste, S., Cenić, M. & Oppel, I. M. Two-step synthesis of hexaammonium
653 triptycene: an air-stable building block for condensation reactions to extended triptycene
654 derivatives. *J. Org. Chem.* **76**, 6389-6393 (2011).
- 655 29 Peng, C. S. & Tokmakoff, A. Identification of lactam–lactim tautomers of aromatic heterocycles
656 in aqueous solution using 2D IR spectroscopy. *J. Phys. Chem. Lett.* **3**, 3302-3306 (2012).
- 657 30 Yang, H. & Craven, B. Charge density study of 2-pyridone. *Acta Crystallogr. Sect. B: Struct. Sci.*
658 **54**, 912-920 (1998).
- 659 31 Case, D. H., Campbell, J. E., Bygrave, P. J. & Day, G. M. Convergence properties of crystal
660 structure prediction by quasi-random sampling. *J. Chem. Theory Comput.* **12**, 910-924 (2016).
- 661 32 Li, P. *et al.* Interpenetration Isomerism in Triptycene-Based Hydrogen-Bonded Organic
662 Frameworks. *Angew. Chem.* **131**, 1678-1683 (2019).
- 663 33 Li, P. *et al.* Assembly of a porous supramolecular polyknot from rigid trigonal prismatic building
664 blocks. *J. Am. Chem. Soc.* **141**, 12998-13002 (2019).
- 665 34 Moulton, B. & Zaworotko, M. J. From molecules to crystal engineering: supramolecular
666 isomerism and polymorphism in network solids. *Chem. Rev.* **101**, 1629-1658 (2001).
- 667 35 Moghadam, P. Z. *et al.* Computer-aided discovery of a metal–organic framework with superior
668 oxygen uptake. *Nat. Commun.* **9**, 1-8 (2018).
- 669 36 Moghadam, P. Z. *et al.* Structure-mechanical stability relations of metal-organic frameworks via
670 machine learning. *Matter* **1**, 219-234 (2019).
- 671 37 Frey, B. J. & Dueck, D. Clustering by passing messages between data points. *Science* **315**, 972-
672 976 (2007).
- 673 38 McInnes, L., Healy, J. & Melville, J. Umap: Uniform manifold approximation and projection for
674 dimension reduction. *arXiv preprint arXiv:1802.03426* (2018).
- 675 39 Pedregosa, F. *et al.* Scikit-learn: Machine learning in Python. *J. Mach. Learn. Res.* **12**, 2825-2830
676 (2011).
- 677 40 Bartók, A. P., Kondor, R. & Csányi, G. On representing chemical environments. *Phys. Rev. B* **87**,
678 184115 (2013).

- 679 41 Jablonka, K. M., Ongari, D., Moosavi, S. M. & Smit, B. Big-Data Science in Porous Materials:
680 Materials Genomics and Machine Learning. *Chem. Rev.* (2020).
- 681 42 De, S., Bartók, A. P., Csányi, G. & Ceriotti, M. Comparing molecules and solids across structural
682 and alchemical space. *Phys. Chem. Chem. Phys.* **18**, 13754-13769 (2016).
- 683 43 Burger, B. *et al.* A mobile robotic chemist. *Nature* **583**, 237-241 (2020).
- 684 44 Häse, F., Roch, L. M. & Aspuru-Guzik, A. Next-generation experimentation with self-driving
685 laboratories. *Trends. Chem.* **1**, 282-291 (2019).
- 686 45 Frisch, M. *et al.* Gaussian 16, Revision A. 03, Gaussian. *Inc.*, Wallingford CT (2016).
- 687 46 Price, S. L. *et al.* Modelling organic crystal structures using distributed multipole and
688 polarizability-based model intermolecular potentials. *Phys. Chem. Chem. Phys.* **12**, 8478-8490
689 (2010).
- 690 47 Stone, A. GDMA: A program for performing distributed multipole analysis of wave functions
691 calculated using the Gaussian program system. *University of Cambridge* (2010).
- 692 48 Pyzer-Knapp, E. O., Thompson, H. P. & Day, G. M. An optimized intermolecular force field for
693 hydrogen-bonded organic molecular crystals using atomic multipole electrostatics. *Acta*
694 *Crystallogr. Sect. B* **72**, 477-487 (2016).
- 695 49 Nyman, J., Pundyke, O. S. & Day, G. M. Accurate force fields and methods for modelling organic
696 molecular crystals at finite temperatures. *Phys. Chem. Chem. Phys.* **18**, 15828-15837 (2016).
- 697 50 Spek, A. Single-crystal structure validation with the program PLATON. *J. Appl. Crystallogr.* **36**, 7-
698 13 (2003).
- 699 51 Chisholm, J. A. & Motherwell, S. COMPACT: a program for identifying crystal structure similarity
700 using distances. *J. Appl. Crystallogr.* **38**, 228-231 (2005).
- 701 52 Willems, T. F., Rycroft, C. H., Kazi, M., Meza, J. C. & Haranczyk, M. Algorithms and tools for high-
702 throughput geometry-based analysis of crystalline porous materials. *Microporous Mesoporous*
703 *Mater.* **149**, 134-141 (2012).
- 704 53 Bondi, A. van der Waals volumes and radii. *J. Phys. Chem.* **68**, 441-451 (1964).
- 705 54 Himanen, L. *et al.* Dscribe: Library of descriptors for machine learning in materials science.
706 *Comput. Phys. Commun.* **247**, 106949 (2020).
- 707 55 Zhao, C. *et al.* Digital navigation of energy–structure–function maps for hydrogen-bonded
708 porous molecular crystals. https://github.com/Yuchees/esf_explorer_templates.
709 doi.org/10.5281/zenodo.4387058 (2020).

710

711

712

713

714

715

716

717

718